The three-dimensional character of a nominally two-dimensional separated turbulent shear flow

By M. P. JAROCH† AND H.-H. FERNHOLZ

Hermann-Föttinger-Institut, Technische Universität Berlin, D-1000, Berlin 12, West Germany

Extensive experiments were performed in the highly turbulent shear layer and in the reverse-flow region downstream of a normal plate followed by a long splitter plate in its plane of symmetry. Whereas the earlier measurements of Ruderich & Fernholz (1986) and Castro & Haque (1987) concentrated on the plane of symmetry (x, y-plane, $z = 0$), the present investigation reveals the full extent of the three-dimensional behaviour of the flow by presenting data in the whole flow field. Spanwise measurements of five components of the Reynolds stress tensor, of integral timescales, and of mean and fluctuating values of the skin friction were carried out by the pulsed-wire technique. Integral lengthscales and spectra outside the reverse-flow region were measured using hot wires. In order to keep three-dimensional effects as small as possible, the aspect ratio was large (model width was 2.55 times the length of the reverse-flow region) and the blockage ratio and free-stream turbulence intensity were low. Despite these efforts the flow investigated here must be considered three-dimensional and classified as both pressure and shear driven. There appears to be a connection between the shape of the reverse-flow region and the level of the fluctuating velocities. Measurements of power spectral densities revealed no flapping motion of the separated turbulent shear layer.

1. Introduction

Most of our knowledge of highly turbulent separated and reattached flow is based on experimental results obtained in nominally two-dimensional flows. These flows are often denoted 'two-dimensional' or 'nominally two-dimensional' because they are generated by a flow past a two-dimensional obstacle, i.e. a body with a uniform cross-section in the spanwise direction.

For high-Reynolds-number flows with separation, reverse flow, and reattachment, three configurations have evolved as test cases: the backward-facing step (e.g. Adams, Johnston & Eaton 1984); the blunt flat plate (e.g. Ota & Itasaka 1976; Kiya & Sasaki 1983, 1985; Cherry, Hillier & Latour 1984); and the flat plate normal to the flow with a long splitter plate (e.g. Ruderich & Fernholz 1986, henceforth denoted by RF; and Castro & Haque 1987).

The latter two configurations have certain advantages. Unlike the flow past a backward-facing step they are hardly influenced by the state of the separating boundary layer. In addition, the separated shear layer leaves the body surface normal to the free stream, thus creating a fairly high and long reverse-flow region and thereby facilitating experimental investigations.

When comparing experimental results obtained in a separating and reattaching

† Present address: Audi AG, Ingolstadt, West Germany.

flow past a two-dimensional obstacle, large differences are found even in such basic properties as the position of the shear layer and the overall level of the Reynolds stresses (see for example the data compiled by Eaton & Johnston 1981). In some cases these differences can be traced to instrumentation problems. It is well known that measurements in regions of instantaneous reverse flow are subject to large errors if standard hot-wire or hot-film anemometry is used to measure the mean velocity or Reynolds stresses, or if hot films and Preston tubes are applied to obtain the skin friction. In these complex flows few experimental results have been obtained by more sophisticated techniques such as pulsed-wire anemometry or laser-Doppler methods.

However, even in cases where adequate instrumentation was used, differences in experimental results have been found. These are probably due to different 'control parameters' such as free-stream Reynolds number, free-stream turbulence intensity, aspect ratio, the thickness of the boundary layer on the tunnel sidewall, and tunnel blockage. These parameters are known to influence the separated flow field in that they affect, for example, the length and the height of the reverse-flow region, the pressure measured at separation and the curvature of the reattachment line in the spanwise direction.

A discussion of the influence of wind-tunnel blockage may be found in Smits (1982) and Ruderich (1985), and of the influence of free-stream turbulence in Cherry (1982), Latour (1983), Kiya & Sasaki (1983) and, more recently, in Nakamura & Ozono (1987).

Three-dimensional effects in these 'nominally two-dimensional' flows have received much less attention. This may be due to the investigation of de Brederode (1975), who investigated the effects of end plates and aspect ratio on the two-dimensionality of the flow past a backward-facing step, a blunt plate, and a forward-facing step. He found that the flow was nominally two-dimensional in his terms if the aspect ratio was larger than 10. The aspect ratio was defined as the ratio of tunnel width or distance between the end plates to the height of the step or the blunt plate. The data compilation of Eaton & Johnston (1981) confirmed nominally two-dimensional flow downstream of a backward-facing step for aspect ratios larger than 10, whereas Cherry *et al.* (1984) claimed a minimum value of 15 for the blunt plate. In the experiments discussed here, aspect ratios A (ratio of B, the length of the normal plate in the z-direction to the fence height h_F above the splitter plate) were 26 and 37, respectively, with the latter value for flow visualization only. Even with these apparently high aspect ratios such a limiting value could not be determined for the T-shaped configurations. It is therefore possible that parameters other than B/h_F may also influence the two-dimensionality of the flow. Figure 1 shows centreline distributions of x_R/h_F, where x_R is the length of the reverse-flow region, plotted against aspect ratio for different blockage ratios β. The curves show that both aspect ratio A and blockage β have a strong influence on x_R/h_F. Thus it may be possible that the ratios x_R/h_F or B/x_R are more suitable parameters for the characterization of the two-dimensionality of the flow over a T-shaped configuration. This latter ratio was 1.33 in the experiment of RF and has been increased to 2.55 (27) and 3.45 (37) in the experiment discussed here. In these cases the flow is by no means nominally two-dimensional but displays instead a curved reattachment line (cf. figure 2) and large variations of the flow field in spanwise direction. Figure 2 shows the topological map of the flow field of the T-shaped configuration in two planes. The main features of the flow agree with those presented in RF and the reader is referred to the earlier paper. The three-dimensionality of the flow field is caused mainly by the two corner vortices formed by the interaction of the sidewall flow, the separated shear layer, and
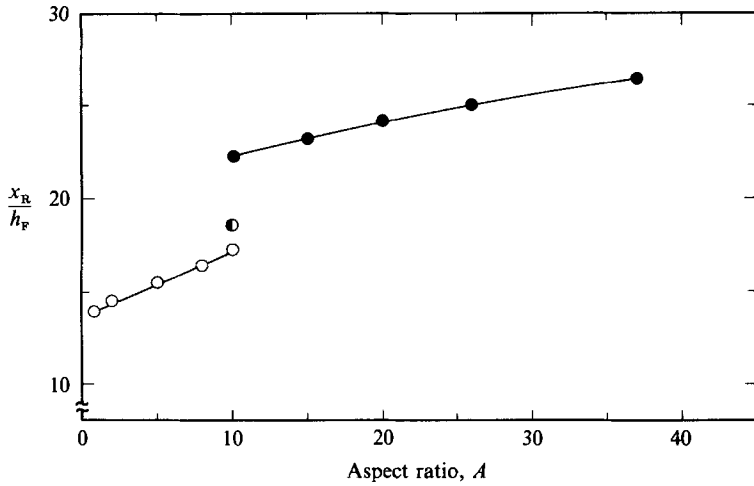
FIGURE 1. Length of the reverse-flow region as a function of aspect ratio A for the T-shaped configuration: $\bigcirc$, Blockage $\beta = 10\%$, $T_u = 0.66\%_\infty$; $\mathbb{O}$, $\beta = 10\%$; $T_u = 0.08\%_\infty$; $\bullet$, $\beta = 3.9\%$, $T_u = 0.08\%_\infty$.
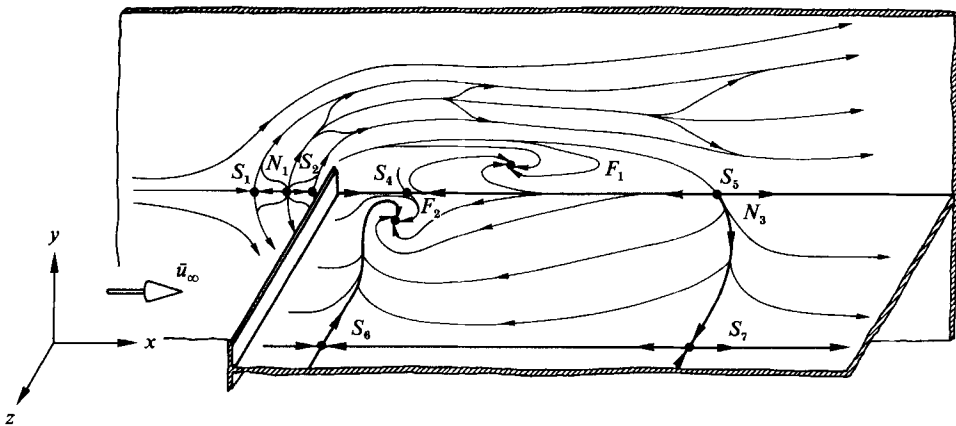

FIGURE 2. Topological map of the flow field.

horseshoe vortices generated in front of the normal plate due to separation of the sidewall boundary layer. It is not to be expected, therefore, that flow-field properties, such as static pressure, skin friction, and mean and fluctuating velocities, will be uniform in the spanwise direction. There appear to be three obvious measures to reduce the strength of the three-dimensionality of the flow:

(*a*) increase the aspect ratio; for a fixed tunnel geometry this means reducing the fence height and therefore the height of the reverse-flow region, in the present experiment making measurements prohibitively difficult;

(*b*) change the direction of the separating flow from 90° in the present experiment to smaller flow angles by tilting the normal plate in the direction of the splitter plate, i.e. perform a different experiment; and finally

(*c*) reduce the effects of the sidewall boundary layer/horseshoe vortices interaction with the separated shear layer and the flow in the reverse flow region.

As option (*c*) was the only feasible approach, we tried to reduce the sidewall effects by inserting end plates; these results were published by Jaroch (1987*b*). Various

Author	Configuration	Re_h	Re_{h_F}	T_u (%)	A	β (%)	d/h	b/B	L/h	x_R/h	x_R/h_F	b/x_R	L/x_R
Ruderich & Fernholz (1986)	Flat plate normal to the flow with splitter plate	3.2×10^4	1.4×10^4	0.66	10.0	10.0	0.12	1.0	32.0	7.52	17.1	1.330	4.26
Castro & Haque (1987)	Flat plate normal to the flow with splitter plate	2.3×10^4	1.1×10^4	0.25	9.0	6.49	0.06	0.72	17.5	9.02	19.2	0.998	1.94
This investigation	Flat plate normal to the flow with splitter plate	3.4×10^4	1.4×10^4	0.08	26.0	2.75	0.185	1.0	37.0	10.20	25.0	2.549	3.63
Cherry et al. (1984)	Blunt flat plate	3.2×10^4	—	0.07	13.2	3.79	1.0	0.838	36.0	4.91	—	2.688	7.33
Kiya et al. (1982) Kiya & Sasaki (1983) Kiya & Sasaki (1985)	Blunt flat plate	2.9×10^4	—	0.3	10.0	5.0 + Adaptive roof	1.0	1.0	25.0	5.00	—	2.000	5.00

TABLE 1. Parameters and their values in four experimental investigations on the structure of turbulent separated shear flows with reattachment

types of end plates, carefully adjusted to the model and the flow direction, were investigated and found to reduce the strength of the corner vortices and the sidewall effects, increasing the straight part of the reattachment line in the centre of the flow field. However, even for the highest aspect ratios investigated, three-dimensional effects govern considerable regions of the flow field of the T-configuration. As shown in figure 6, a reduction of the aspect ratio and the use of end plates leads to a more strongly curved reattachment region than for the case of the largest possible aspect ratio without end plates. A larger aspect ratio can be achieved without end plates, as the presence of the plates reduces the effective spanwise dimension of the tunnel. The present investigation used the full span of the tunnel and no end plates.

These considerations have led to an investigation of the effects of the three-dimensionality of the flow on the characteristic properties of the flow field using the largest feasible aspect ratio, small blockage, and a low turbulence level. From these measurements we hoped to be able to generalize the results, at least for a practically interesting range of aspect ratios, by showing which flow quantities were affected most.

Dimensional analysis suggests that the parameters shown in table 1 should characterize the flow around the T-configuration. For comparison the table includes recent investigations on turbulent flows with separation and reattachment.

The notation is as follows: B and H are the width and height of the test section, L and d the length and thickness of the splitter plate, h and h_F the total height of the normal plate and its height above the splitter plate, b the distance between end plates, x_R the length of the reverse-flow region. A is the aspect ratio, β the blockage ratio and $T_u = (\overline{u'^2})^{\frac{1}{2}}_{\infty}/u_{\infty}$ the turbulence level.

The experimental programme outlined is presented in detail. Section 2 describes the experimental apparatus and the measuring techniques with the emphasis on the pulsed-wire technique. This is followed in §3 by an extensive presentation of the behaviour of wall and field measurements in the spanwise direction and a possible explanation for the existence of the high intensities in this three-dimensional flow field. Section 4 contains the conclusions.

2. Experimental apparatus and measuring techniques

The wind tunnel used for these experiments was the closed-return low-speed wind tunnel of the Hermann-Föttinger-Institut. The tunnel is driven by an axial fan with blades of variable pitch and powered by a 0.5 MW d.c. motor. Motor and fan are mounted between two sets of sound mufflers. The settling chamber contains three screens and a non-woven filter cloth mounted onto the first screen. The contraction reduces the square cross-section of the settling chamber to the rectangular cross-section of the test section and has a contraction ratio of 6.25:1.

The test section has a cross-section of 1.4×2.0 m^2 and a length of 10 m. It consists of four interchangeable boxes. The model was mounted into the third box so that the separation line on the plate normal to the flow (position $x = 0$) was 5280 mm downstream of the end of the wind-tunnel contraction. At this position the thickness δ of each of the tunnel boundary layers on the top and bottom walls, was 150 mm, or 10.7 % of the model span. The mean velocity profile outside the tunnel boundary layer was constant within 1 % of the mean velocity, and the turbulence intensity was 0.1 % over the frequency range d.c. to 40 kHz.

The model was mounted vertically (figure 3) to avoid problems with model bending due to its weight; it spanned the tunnel height. The splitter plate was made
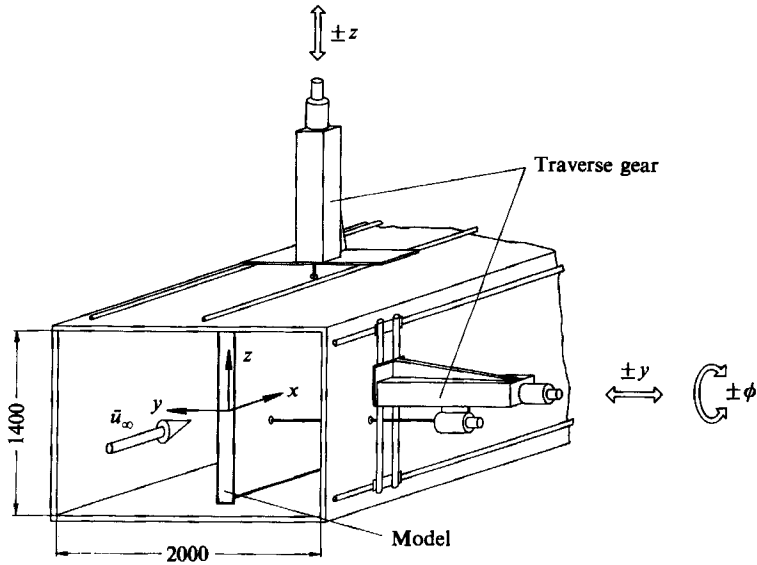
FIGURE 3. Sketch of the model and the traverse gear mounted in a test section box of the wind tunnel.

of two separate plates 10 mm thick, ALCA-PLUS, each 1.4×1.0 m². The upstream plate could be turned by 180° about the axis normal to its surface to allow for two orientations of the probes mounted on it with respect to the leading edge. Each plate had a slot along the line of symmetry into which different PVC inserts could be mounted, with pressure tappings or holes for the traverse gear. The upstream plate had, in addition, 18 holes to hold instrumentation ports.

The plate normal to the flow was made of a steel bar of $B = 1.4$ m, 6 mm thick and $h = 54$ mm resulting in a height over the surface of the splitter plate of $h_{\mathrm{F}} = 22$ mm. The edge of the bluff plate was machined to a sharp 25° bevel. This plate could be removed and replaced by a profiled leading edge (Hancock 1980) followed by a DYMO-tape V-band tripping device for calibration purposes. In order to produce a flow symmetrical about the upper and lower surfaces of the splitter plate, three movable flaps were fitted at the downstream end. These flaps had to be set at an angle of 10° to obtain a symmetrical flow field. Symmetry with respect to the centreline of the flow was obtained by adjusting the model about the y-axis until the mean pressure field on the surface of the splitter plate was symmetric about the line $z = 0$. Even very small changes in the 'yaw angle' of the plate system ($\approx 0.1°$) resulted in large changes of the surface pressure field.

Probes were moved by means of two traverse gears outside the wind tunnel. One traverse provided motion in all three linear directions and allowed rotation about the y-axis; the y-direction translation and the rotation were computer automated, whereas the other two degrees of freedom were controlled manually. The second traverse also provided three linear degrees of freedom, with only the z-direction automatically controlled. Computer controlled automatic movements had a resolution in a linear direction of 10^{-6} m and in an angular direction of 0.2°.

Hot wires were used where possible and pulsed wires where necessary. Hot-wire measurements were carried out using a Prosser Scientific Instruments PSI 6110 anemometer interfaced to a Commodore 3032 microcomputer via a 10-bit AD

Measured variable	Method of measurement	Position of measurement	Measurement error	Repeatability (%)	Resolution
Angle about the y-axis	10-turn potentiometer	—	1%	99.5	0.2°
Distance from walls	Optical	—	0.1 mm	98	10^{-6} mm
$\bar{p}_\infty$	Mercury barometer	—	0.1%	100	0.1 mbar
$\bar{T}_\infty$	Electronic thermometer	—	2%	99	0.1 K
$\bar{p}$	FV-micromanometer	—	2%		0.005 kp/m²
$\bar{u}$			2%		
$\bar{v}, \bar{w}, \overline{u'^2}, \overline{v'^2}, \overline{w'^2}, \overline{u'v'}, \overline{u'w'}$	Hot wire	Separated shear layer	10%	98	
		Reattached region	5%		
$u, \bar{\tau}_w, \chi$	Pulsed wire	Separated shear layer	15%	98	
$\overline{v'^2}, \overline{\tau_w'^2}$		Reattached region	8%	97	
S, K			5%		
$\overline{v'^2}, \overline{w'^2}, \overline{u'v'}, \overline{u'w'}$	Pulsed wire	—	10%	97	
			15%	95	
			20%	92	
$A_{11}^{(2)}, A_{11}^{(3)}$	Hot wire	$T_u > 15\%$	8%	98.5	0.1 mm
		$T_u \le 15\%$	13%		
$A_{11}^{(2)}$	Pulsed wire		13%	97	0.1 ms

TABLE 2. Estimates of measurement errors

converter. All measurements were taken digitally using 10 000 samples per point, except for the power spectral density and the coherence functions which were measured by means of a Wavetech/Rockland cross-channel analyser. The probes were HFI-standard normal- and ×-wire probes. The hot-wire probes and their error estimates have been described by Fernholz & Vagt (1981).

Pulsed-wire measurements (Bradbury & Castro 1971) were performed by a modified PELA Flow Instruments anemometer (Wagner 1986) interfaced to a CBM 3032 microcomputer. The velocity probes were HFI-pulsed-wire probes of the 'large type' (Jaroch 1985). Reynolds stresses in the (x, y)- and the (x, z)-planes were measured with the special slanted pulsed-wire probe described by Jaroch & Dahm (1987) – see also Castro & Cheun (1982) – and measurements of the autocorrelation coefficients of the fluctuating velocity coordinate u' were performed employing the pulsed-wire procedure of Castro (1985).

Hot wires and pulsed wires were calibrated in the free stream of the test section without the normal plate in position. The calibrations were checked after each profile measurement and, if the values of the calibration were found to be suspect, the measurements were discarded. Integration time for the hot wires was ≈ 60 s.

Fluctuating and mean values of skin friction were measured using a pulsed wall probe (Castro & Dianat 1983) which was calibrated directly against a Preston tube in the zero-pressure-gradient turbulent boundary layer on the splitter plate with a faired leading edge. The calibration of the probe is described by RF and its design by Dengel, Fernholz & Hess (1987). The sensor wires had a smaller active length (0.5 mm) than the probe used by RF, thus permitting a better spatial resolution of the wall shear-stress fluctuations.

Static pressure was measured by pressure orifices (0.5 mm diameter) along the centreline, at various positions in the spanwise direction on the splitter plate, and on the front part of the normal plate. The pressure tappings were connected via a Scanivalve to an automatic micromanometer (Froebel & Vagt 1974).

The free-stream Reynolds number, $Re_{h_\mathrm{F}} = 1.4 \times 10^4$, was monitored by a Pitot-static tube at a reference location 4 m upstream of the normal plate. The free-stream velocity at the normal plate $(x = 0)$ was about 6 % higher than that at the reference position.

A detailed discussion of the resolution, the repeatability, and the measurement error for the different techniques in different regions of the flow field is given by Jaroch (1987a), as summarized in table 2. By 'measurement error' we mean an interval about the measured value of a variable which is likely to contain the true value of the variable. The width of the interval is given as a fraction of the measured value. By 'repeatability' we mean the degree to which successive measurements of a variable are identical.

3. Measurements of wall and field variables in the reverse-flow region and downstream of reattachment

Three-dimensional turbulent shear flows can be generated by pressure differences, shear stresses, or large vortex structures interacting with the main flow. The three-dimensionality of the flow described here has been caused by all three effects and it will be impossible – unless a very generous measuring programme can be financed – to separate these effects from each other and from parameters such as blockage and aspect ratio mentioned above. The description of the measurements will therefore be divided into two sections. First, we shall present field measurements of $\bar{c}_p$ and $\bar{c}_f$
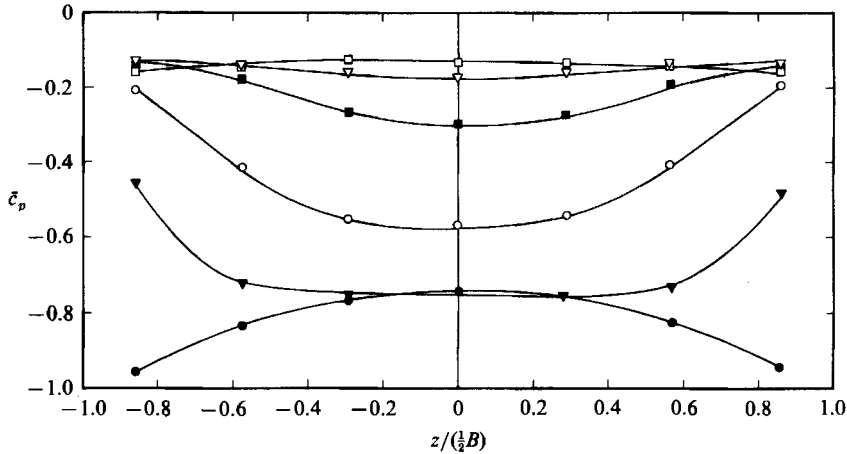
FIGURE 4. Spanwise distributions of the mean static-pressure coefficient on the surface of the splitter plate: ●, $x/x_R = 0.2$; ▼, 0.56; ○, 0.72; ■, 0.92; ▽, 1.09; □, 1.45.

followed by more detailed measurements along the centreline (x, y-plane, $z = 0$) of the splitter plate. Finally, a display of the three-dimensional behaviour of the flow field off the centreline in the spanwise direction will be given. Owing to limitations of space only a selection of data can be presented and the reader is referred to Jaroch (1987a) for details. The results of this investigation show that the centreline is a line of symmetry in a wholly three-dimensional flow.

3.1. *The mean static-pressure field*

The mean static-pressure distribution in the spanwise direction (figure 4) is given for several x-locations in the reverse-flow region and downstream of reattachment. The usual pressure coefficient, $\bar{c}_p = (\bar{p} - p_\infty)/(0.5\rho u_\infty^2)$, is plotted against the dimensionless spanwise coordinate z.

The distribution at $x/x_R = 0.2$ is determined by the two corner vortices (cf. figure 2) which are low-pressure regions. Flow visualization experiments using the surface oil-flow technique showed that the rate of rotation of these corner vortices and thus their strength and the pressure in their centre depend on the thickness of the wind-tunnel wall boundary layer. When end plates were used, the vortices rotated much more slowly compared with the case when the model spanned the entire width of the test section. This did not depend on whether or not the end plates extended upstream of the model. It is therefore concluded that the strength of the vortices is controlled by the interaction between the separated shear layer and the wind-tunnel wall boundary layer. The strength of the interaction will again control the pressure level in and near these vortices which cause the pressure to remain lower than near the centreline (filled circles). The addition of end plates and therefore a reduction in the effective boundary-layer thickness only weakens this pattern but does not change its nature. Further downstream, owing to the strong secondary flow in the corner region between the splitter plate and the sidewall, the static pressure increases sharply near the sidewalls (filled triangles) and leads to earlier flow reattachment than on the centreline, resulting in a curved reattachment line (see also figure 7 for the skin-friction distributions).

Downstream of reattachment ($x/x_R = 1.09$, open triangles) the pressure field
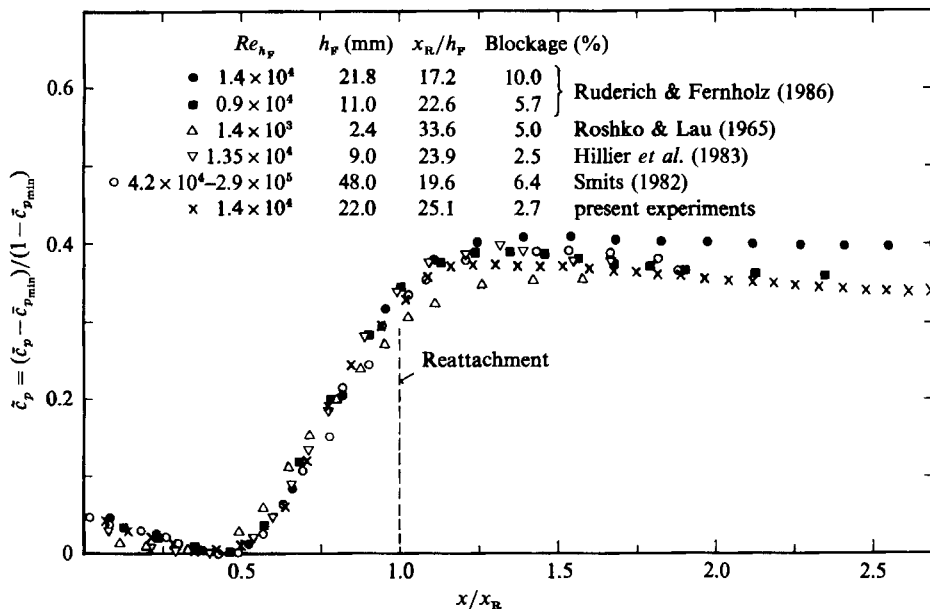
FIGURE 5. Development of the pressure coefficient along the centreline of the splitter plate.

becomes almost uniform across the span of the splitter plate. This rapid return to uniformity differs from the behaviour of all other flow quantities discussed here. The pressure distribution along the centreline is shown in figure 5, using the modified pressure coefficient $\tilde{c}_p$ suggested by Roshko & Lau (1965). The present results agree well with the distributions shown in RF's figure 7 and coincide with their lower-blockage case in the region $x/x_R > 1$.

3.2. *Reattachment region and skin-friction distribution*

As was mentioned above, one of the most obvious manifestations of the three-dimensionality of the flow is the curved reattachment line. It is defined as the locus of points on the splitter plate at the downstream end of the reverse-flow region where the x-component of the mean skin-friction vector is zero. Figure 6 shows the reattachment line for the available experiments, where the lateral direction is normalized by the reattachment length x_R on the centreline of the splitter plate. Irrespective of the aspect ratio, which ranges from 9 to 37, all flows show curved reattachment lines, implying they are a common feature of the flow field generated by the T-configuration. The smallest curvature is obtained in the experiment with the largest aspect ratio (filled squares, $A = 37$), i.e. here the end effects are smallest (the same ratio of δ/B as for $A = 26$). The effect of the introduction of end plates with the reduction of the aspect ratio to 15 (other parameters unchanged) is shown by the open squares; the curvature does not increase significantly. So the 'positive' effect of end plates in reducing the thickness of the sidewall boundary layer may be counteracted by the reduction of the aspect ratio. Still another effect may be seen by a comparison of the experiments of Castro & Haque and RF where the aspect ratios were similar (table 1) but only the first authors used end plates. The curvature of their reattachment line is even slightly larger than that seen by RF.

Although the aspect ratio of the present experiment (filled circles) exceeded that of RF by a factor of 2.6 the distributions of $x_R/x_{R\phi}$ are almost the same. Our
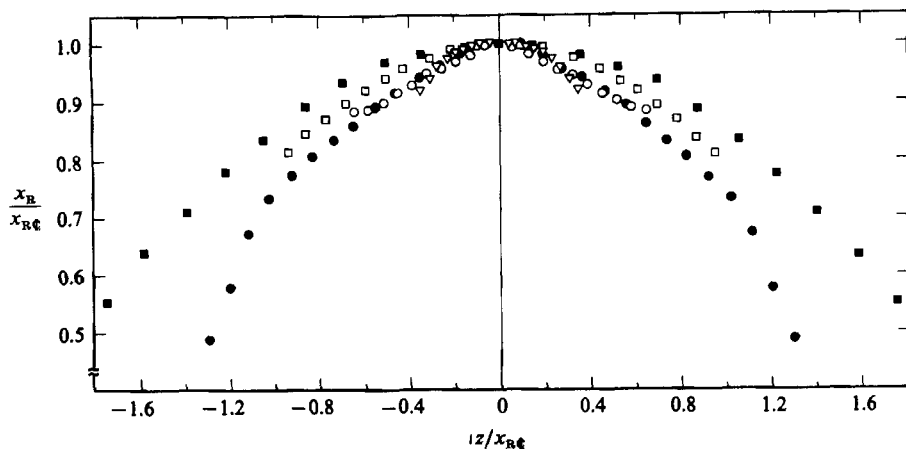
FIGURE 6. Spanwise reattachment line: $\bigcirc$, Ruderich & Fernholz (1986); $\bigtriangledown$, Castro & Haque (1987); $\bullet$, this experiment; $\blacksquare$, $A = 37$, $\beta = 3.6\%$, $T_u = 0.1\%$, no endplates; $\square$, $A = 15$, $\beta = 3.6\%$, $T_u = 0.1\%$, with endplates.
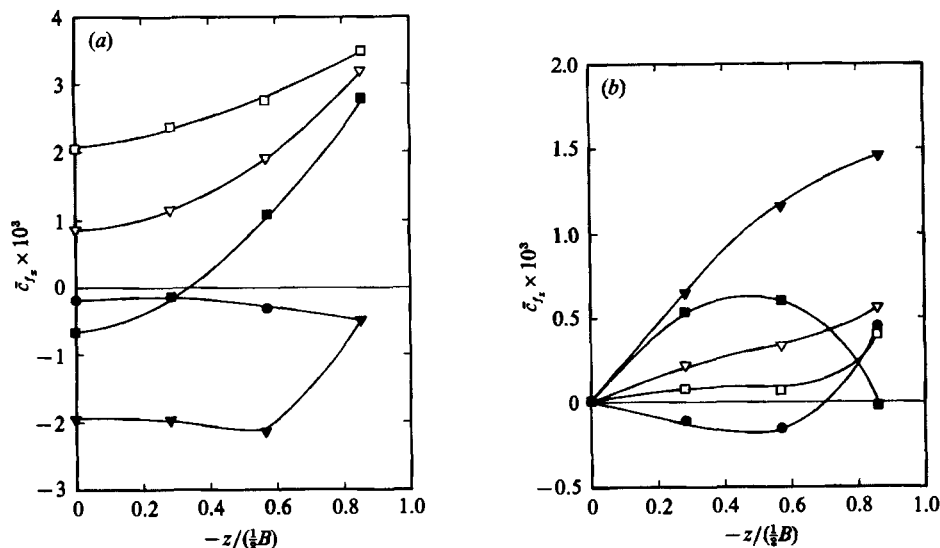

FIGURE 7. Three-dimensional behaviour of the x- and z-coordinate of the mean wall-shear-stress coefficient on the splitter plate: $\bullet$, $x/x_R = 0.2$; $\blacktriangledown$, 0.56; $\blacksquare$, 0.92; $\bigtriangledown$, 1/09; $\square$, 1.45.

conclusion here is that, although end plates might have reduced the effects of three-dimensionality, they would not have eliminated them altogether.

Figures 7 (a) and 7 (b) show the three-dimensional behaviour of the x- and the z-component of the mean skin-friction coefficient, respectively, where $\bar{c}_{f_i} = 2\bar{\tau}_{w_i}/(\rho u_\infty^2)$ and $\bar{\tau}_w$ is the mean wall shear stress. $\bar{c}_{f_x}$ and $\bar{c}_{f_z}$ show considerable variation in the lateral direction. Immediately downstream of reseparation the component in the z-direction is of the same order as the component in the main flow direction; further on, $\bar{c}_{f_z}$ is almost everywhere smaller than $\bar{c}_{f_x}$, with the obvious exception of the reattachment region. The spanwise variation of $\bar{c}_{f_z}$ is still about 50\% at $x/x_R = 1.45$, in contrast to the spanwise pressure distribution but in agreement with the slow
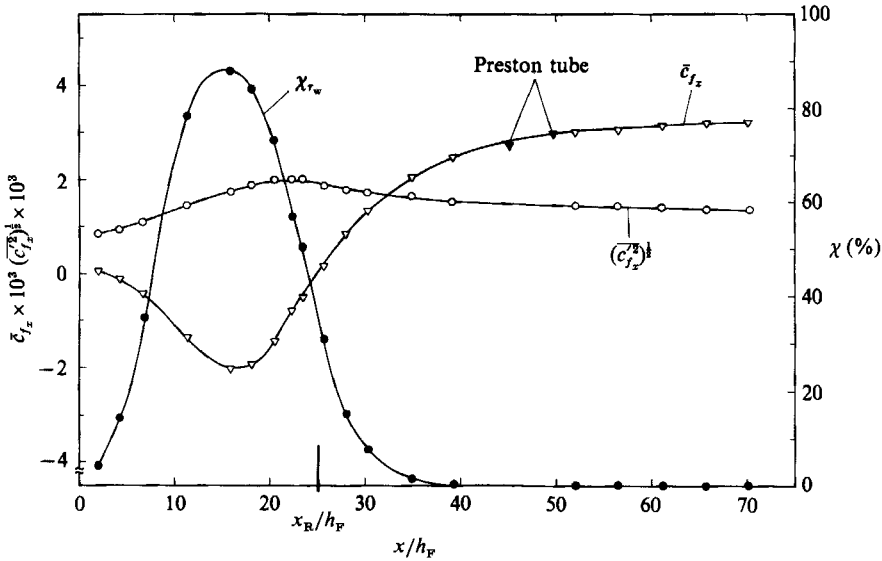
FIGURE 8. Distribution of mean value, fluctuation intensity and reverse-flow parameter of the
wall shear stress along the centreline of the splitter plate.

readjustment of the other flow quantities (see RF and below). The larger values at the sides of the splitter plate are due to the development of the reattached shear layer over a larger distance than along the centreline.

Figure 8 presents the development of the mean and fluctuating skin friction and of the reverse-flow parameter χ_w along the centreline of the splitter plate, with

$$\chi_w = \int_{-\infty}^{0} p(\tau_{w_x}) \, d\tau_{w_x},$$

where $p(\tau_{w_x})$ is the probability density function of the distribution of the instantaneous shear stress.

While the overall features of this development are similar to those observed by RF and by Castro & Haque (1987), there are some differences. The minimum skin friction, which occurs at about $x/x_R = 0.6$, is lower in the present work $(\bar{c}_{f_{min}} = -1.65 \times 10^{-3})$ than that measured by RF $(\bar{c}_{f_{min}} = -3.3 \times 10^{-3})$ or by Castro & Haque (1987) $(\bar{c}_{f_{min}} = -3.6 \times 10^{-3})$.

The same trend is observed in the maximum strength of the skin-friction fluctuations; it is lower in the present experiment $(\overline{c_{f_x}'^2})^{\frac{1}{2}}_{max} = 2 \times 10^{-3}$, compared to 2.6×10^{-3} and 3×10^{-3} measured by RF and Castro & Haque, respectively. The probe used in the present experiment had a higher spatial resolution than that of RF, for example, and would have shown higher values, had they been present. The reverse-flow parameter χ_w does not exceed 87%, which is lower than the value measured by RF (cf. their figure 8).

The 'turbulence intensity of the skin friction' $(\overline{c_f'^2})^{\frac{1}{2}}/\bar{c}_f$ in the centre of the reverse-flow region $(x/x_R = 0.5)$ shows a trend which will be found again in the distribution of the velocity fluctuations. The intensity peaks at 115% in this flow, compared with 62% and 72% in the experiments of Castro & Haque (1987) and RF, respectively.

This is one indication that the flow with parameters selected to minimize the influence of aspect ratio and blockage shows higher fluctuation levels than the flow
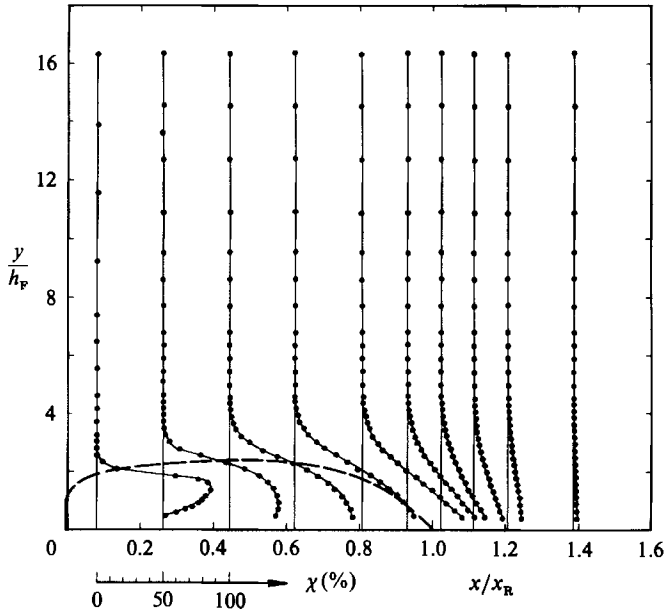
FIGURE 9. Development of the profiles of the reverse-flow parameter χ along the centreline of the splitter plate (pulsed-wire data). The dashed line represents the locus of $\bar{u} = 0$.

past a similar configuration with higher blockage and/or lower aspect ratio. We shall return to this point later.

3.3. *The distribution of mean velocity and Reynolds stress profiles*

Measurements were made of the mean velocity field, $\bar{u}$, $\bar{v}$ and $\bar{w}$, and of five of the six components of the Reynolds stress tensor, $\overline{u'^2}$, $\overline{v'^2}$, $\overline{w'^2}$, $\overline{u'v'}$ and $\overline{u'w'}$. The sixth component, $\overline{v'w'}$, was not measured because the pulsed-wire measurements would be difficult and have a large uncertainty. All data were taken by means of pulsed-wire probes, and measurements of $\overline{v'^2}$, $\overline{w'^2}$ and $\overline{u'v'}$ differ from the hot-wire results of RF in the inner part of the separated shear layer. An estimate given by Castro & Haque (1987) provides some insight into why $\times$-wire data are too low in this region of the flow. Only centreline measurements are presented here: see §3.6 for a discussion of the spanwise variations of these quantities.

Figure 9 presents profiles of the reverse-flow parameter χ along the centreline of the splitter plate. These profiles give an indication of the regions of the flow in which normal hot-wire probes may be used without rectification errors.

Figures 10–13 show sequences of profiles of $\overline{u'^2}$, $\overline{v'^2}$, $\overline{w'^2}$ and $\overline{u'v'}$, respectively, through the reverse-flow and the reattachment region. Full circles indicate pulsed-wire data and open circles hot-wire measurements. Qualitatively they confirm the Reynolds stress distributions presented by RF, but attention is again drawn to the differences between measurements obtained by the pulsed-wire and the hot-wire technique as far downstream as $x/x_{\rm R} = 1.4$. This means that all previous hot-wire measurements presented in the literature for the reattachment region – and not only for the T-configuration – should be regarded with caution.

For some distance downstream of reattachment, the effects of the instantaneous reverse flow in the near-wall region and the adaptation of the reattaching shear layer to the wall boundary condition combine to produce a mean velocity profile that does
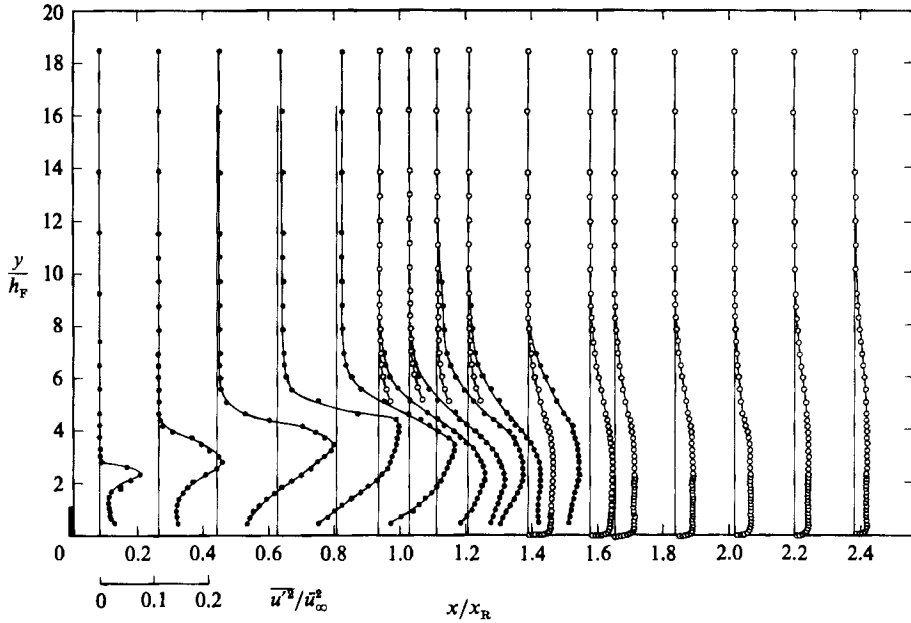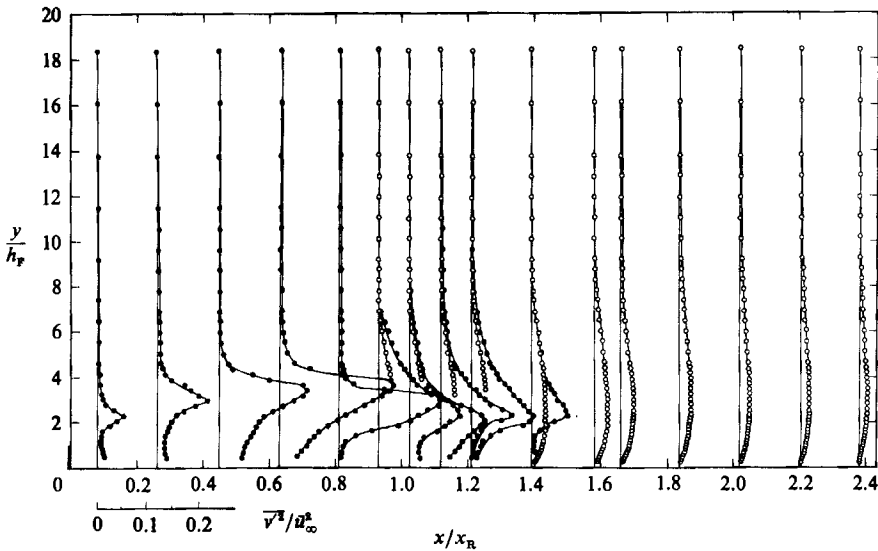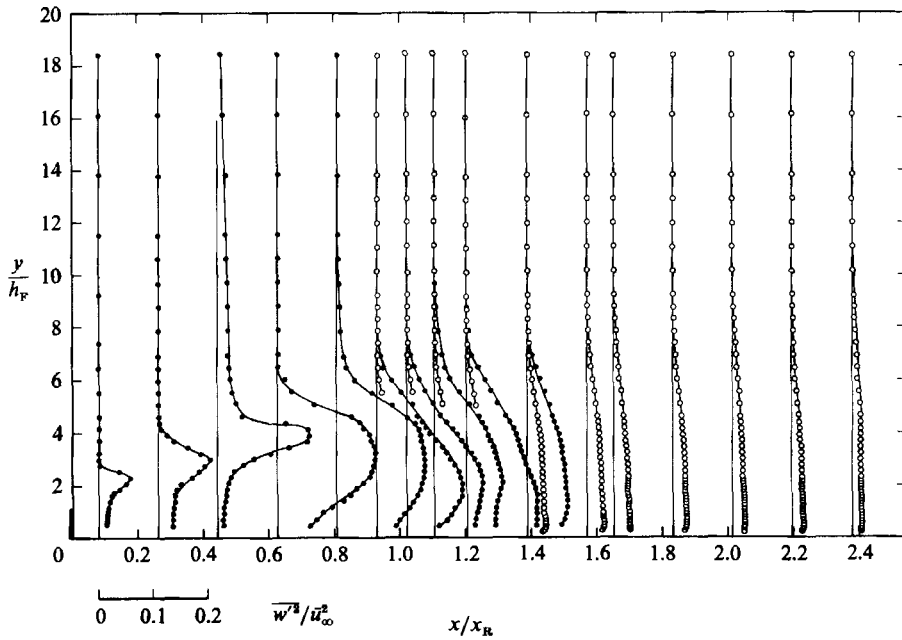
FIGURE 10. Development of the profiles of the intensity of the Reynolds normal stress $\overline{u'^2}$ along the centreline of the splitter plate: $\bigcirc$, hot-wire data; $\bullet$, pulsed-wire data.

FIGURE 11. Development of the profiles of the intensity of the Reynolds normal stress $\overline{v'^2}$ along the centreline of the splitter plate. Symbols as figure 10.

not fit the logarithmic law of the wall (figure 14). The logarithmic region grows from near the wall into the attached shear layer with downstream distance but the velocity profile is not characteristic of that in a typical undisturbed boundary layer even as far downstream as $x/x_R = 2.38$. All profiles, however, display the usual linear region in the vicinity of the wall, even immediately downstream of reattachment.

FIGURE 12. Development of the profiles of the intensity of the Reynolds normal stress $\overline{w'^2}$ along the centreline of the splitter plate. Symbols as figure 10.
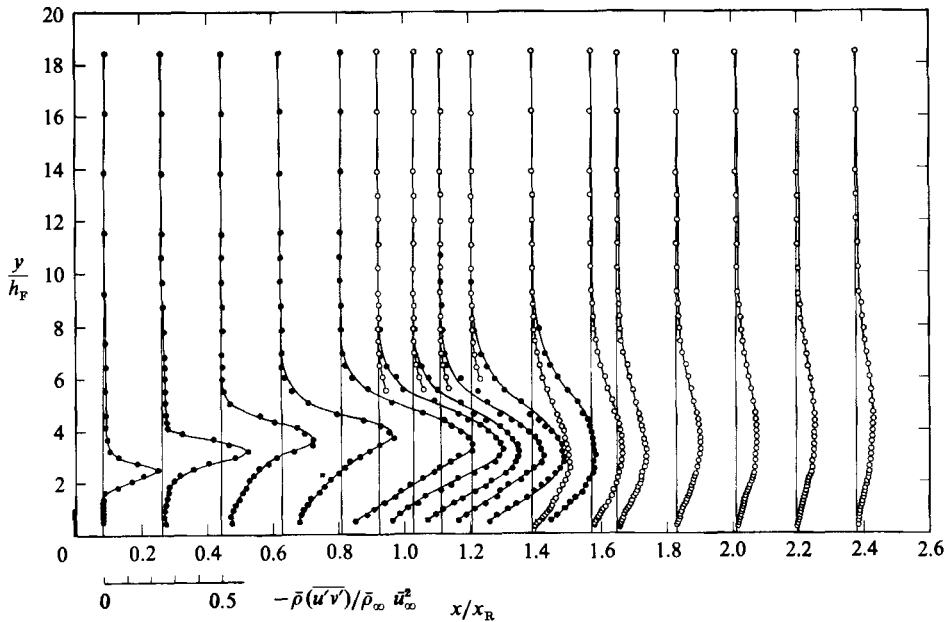
FIGURE 13. Development of the profiles of the Reynolds shear stress $-\overline{\rho u'v'}$ along the centreline of the splitter plate. Symbols as figure 10.
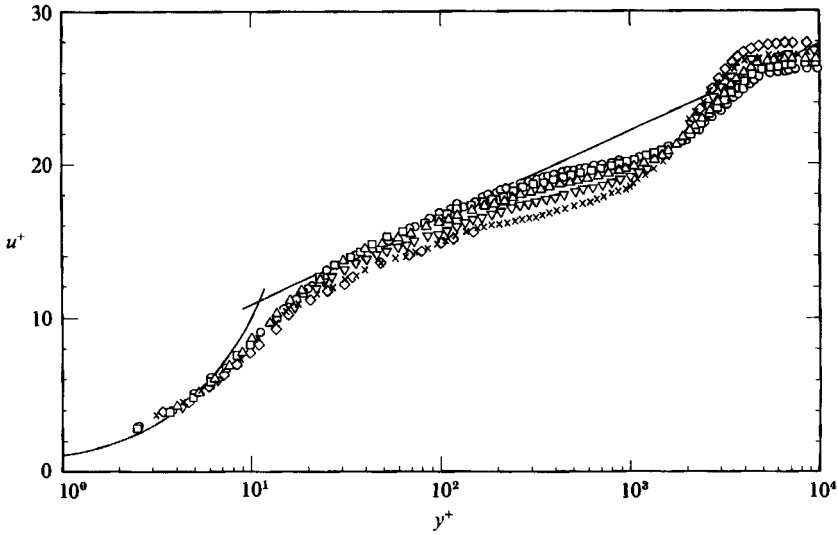
FIGURE 14. Comparison of the law of the wall with velocity profiles in a wall-bounded turbulent shear flow downstream of reattachment: $\Diamond$, $x/x_R = 1.57$; $\times$, 1.65; ∇, 1.83; $\triangle$, 2.01; $\square$, 2.19; $\bigcirc$, 2.38.
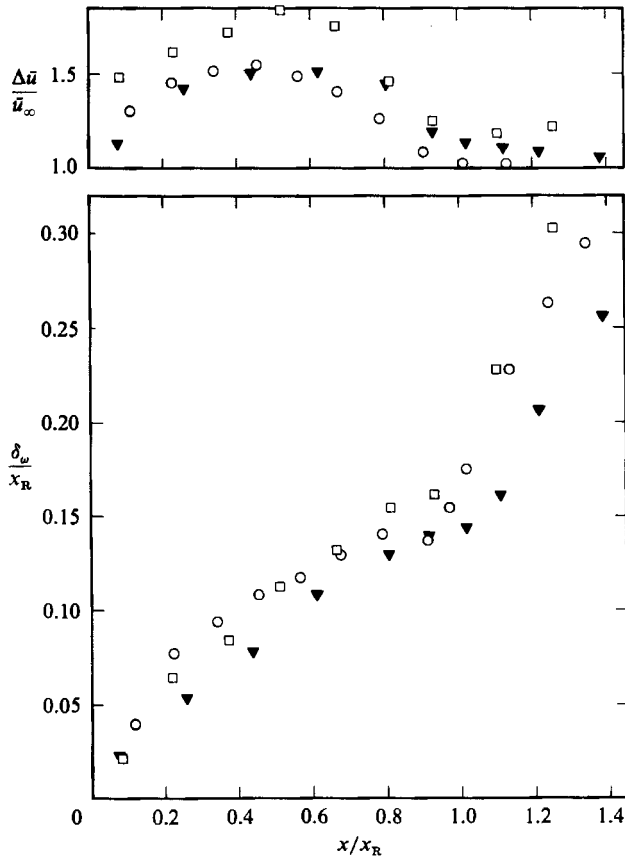
FIGURE 15. Development of the shear-layer thickness (maximum slope thickness) along the centreline of the splitter plate: $\square$, Ruderich & Fernholz (1986); $\bigcirc$, Castro & Haque (1987); $\blacktriangledown$, this investigation.
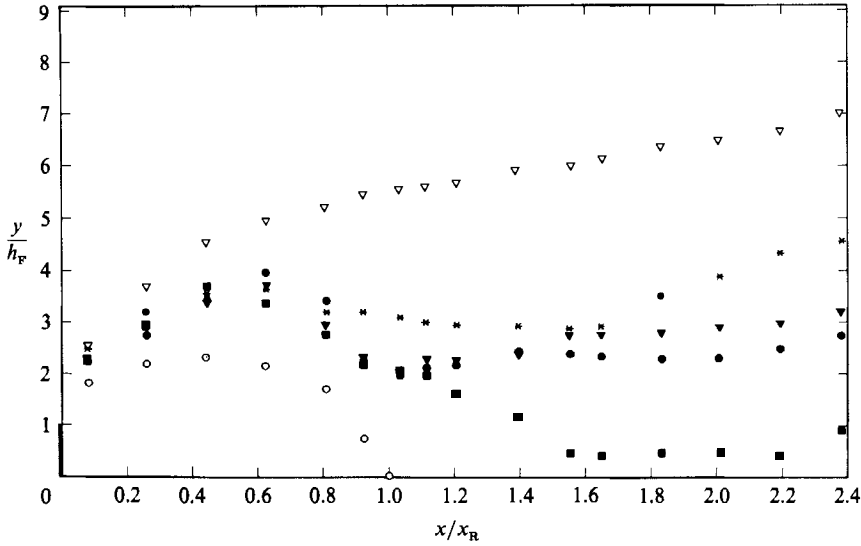
FIGURE 16. Development of the position of the maxima of the specific Reynolds stresses along the centreline of the splitter plate: $\triangledown$, $y = y\,(T_u = 10\%)$; $\bigcirc$, $y = y\,(\bar{u} = 0)$; $\bullet$, $y = y\,(\overline{u'^2_{\max}})$; $\blacktriangledown$, $y = y\,(\overline{v'^2_{\max}})$; $\blacksquare$, $y = y\,(\overline{w'^2_{\max}})$; $*$, $y = y\,(\overline{u'v'_{\max}})$.

The mean-velocity measurements permit the calculation of the vorticity thickness δ_ω, defined by Brown & Roshko (1974) as

$$\delta_\omega = \frac{\bar{u}_{\max} - \bar{u}_{\min}}{(\partial\bar{u}/\partial y)_{\max}} = \frac{\Delta\bar{u}}{(\partial\bar{u}/\partial y)_{\max}},$$

where $(\partial\bar{u}/\partial y)_{\max}$ was evaluated between the locations of $\bar{u}_{\min}$ and $\bar{u}_{\max}$. δ_ω/x_R (with $x_R = 550$ mm) is plotted against x/x_R in figure 15 and compared to the measurements of RF and Castro & Haque (1987). In contrast to RF, the other two sets of experiments do not confirm a roughly linear growth of the vorticity thickness but show a gradually reducing growth rate down to reattachment. It appears that the vorticity thickness is dependent on the blockage ratio and the aspect ratio – and possibly on the turbulence level of the flow – which are different in the three experiments. The distributions of $\Delta\bar{u}/u_\infty$ in the upper part of figure 15 (where $\Delta\bar{u} = \bar{u}_{\max} - \bar{u}_{\min}$) differ by not more than 20% and this cannot explain the different behaviour of the δ_ω-distributions. So far we have not enough evidence for an explanation.

Figure 16 shows the loci of the maxima of the Reynold stresses, the locus of $\bar{u} = 0$, and the locus of $T_u = 10\%$ along the centreline of the splitter plate. The behaviour of the loci is generally in agreement with that observed by RF: the maxima of all measured components of the Reynolds stress tensor occur at approximately the same distance from the splitter plate for the first 80% of the separated shear layer. After reattachment the locus of the maximum of the Reynolds shear stress $\overline{u'v'}$ increases its distance from the wall with increasing x, while the maxima of the normal stresses remain at approximately constant distances above the wall (2–3 fence heights for $\overline{u'^2_{\max}}$ and $\overline{v'^2_{\max}}$ and about 0.5 fence heights for $\overline{w'^2_{\max}}$).

The maximum values of the Reynolds stresses along the centreline are plotted in figure 17. The normal stresses and $\overline{u'v'}$ rise for the first 60% of the length of the reverse-flow region and then fall to approximately 20% of their respectively absolute
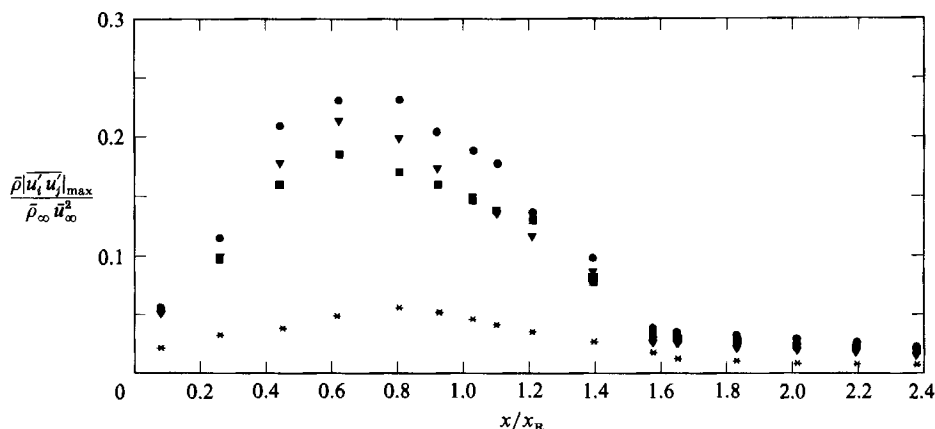
FIGURE 17. Development of the maxima of the specific Reynolds stresses along the centreline of the splitter plate: ●, $(\overline{u'^2_{max}})$; ▼, $(\overline{v'^2_{max}})$; ■, $(\overline{w'^2_{max}})$; *, $(\overline{u'v'_{max}})$.

Author	Castro & Haque (1987)	Ruderich & Fernholz (1986)	This investigation
$\overline{u'^2_{max}}/\overline{u}^2_\infty$	0.09	0.13	0.22
$\overline{v'^2_{max}}/\overline{u}^2_\infty$	0.07	0.04	0.20
$\overline{w'^2_{max}}/\overline{u}^2_\infty$	0.07	0.05	0.18
$-\overline{u'v'_{max}}/\overline{u}^2_\infty$	0.03	0.02	0.05
$y(\overline{u'^2_{max}})/x_R$	0.10	0.15	0.17
$\overline{v'^2_{max}}/\overline{u'^2_{max}}$	0.75	0.28	0.93
$\overline{w'^2_{max}}/\overline{u'^2_{max}}$	0.79	0.37	0.80
$-\overline{u'v'_{max}}/\overline{u'^2_{max}}$	0.34	0.17	0.24

TABLE 3. Comparison of the maximum turbulence intensities measured in the experiments of Ruderich & Fernholz (1986), Castro & Haque (1987) and in this investigation

maximum value at about $1.5x_R$. The high degree of anisotropy in the turbulence structure upstream of reattachment decays rather quickly, and downstream of $x/x_R = 1.6$ all normal stresses maintain approximately constant ratios.

Table 3 gives a comparison of the absolute maxima of the fluctuation intensities and the Reynolds shear stress. The measurements of RF show rather low values for $\overline{v'^2_{max}}$, $\overline{w'^2_{max}}$ and $-\overline{u'v'_{max}}$, owing to the use of the hot-wire technique as was noted by Castro & Haque (1987). In comparing the ratios of the absolute maxima of the Reynolds stresses of this investigation with those of Castro & Haque (1987), differences can be explained to some degree by the uncertainties of the pulsed-wire measurements. However, the discrepancies in the maxima of the streamwise fluctuations, measured using the pulsed-wire technique in all three experiments, are larger than the estimated uncertainty in the measurements: $\overline{u'^2_{max}}/u^2_\infty = 0.22$ (present experiment), 0.13 (RF), and 0.09 (Castro & Haque 1987). These different levels may be connected to the different shapes of the reverse-flow region in the three flow configurations. In the present experiment the separated shear layer is less curved immediately downstream of separation than the shear layer of RF, for example, and reaches much further out into the flow. If the maximum distance y of the locus of $\overline{u'^2} = \overline{u'^2_{max}}$ from the surface of the splitter plate is defined as the maximum height of

the reverse-flow region, a 'bubble slenderness ratio' may be defined as $x_R/y_{\overline{u^2_{max}}}$. This value is 6.1 in the present investigation and 6.4 and 9.8 in the flow configurations of RF and Castro & Haque (1987), respectively.

A comparison between the data of the present experiment and that of Castro & Haque shows that increasing the aspect ratio A by a factor of 3 and decreasing blockage by a factor of 2 (table 1) approximately doubles the maximum values of $\overline{u'^2}$ and $\overline{u'v'}$ and triples those of $\overline{v'^2}$ and $\overline{w'^2}$. This leads to the conclusion that a higher aspect ratio and lower blockage increase all fluctuating quantities along the centreline in the reverse-flow region and probably also in spanwise direction. We believe that these two parameters dominate over that of the sidewall boundary layer, which nevertheless may exert a strong local effect.

3.4. *The integral scales of the flow field*

The figures described in this subsection present the results of the measurements of the spatial correlation coefficients

$$R_{11}^{(i)} = \frac{\overline{u'(x+re_i)\,u'(x)}}{(\overline{u'^2}(x+re_i)\,\overline{u'^2}(x))^{\frac{1}{2}}}$$

(where r is the separation in the direction of the unit vector e_i), and the autocorrelation coefficient

$$R_{11}^{(t)} = \frac{\overline{u'(t+\tau)\,u'(t)}}{(\overline{u'^2}(t+\tau)\,\overline{u'^2}(t))^{\frac{1}{2}}}$$

of the longitudinal velocity fluctuations u'. Correlation coefficients are not shown here (they may be found in RF and Jaroch 1987a) but profiles of the respective integral scales

$$\varLambda_{11}^{(t)} = \int_0^{r(R_{11}^{(t)}=0)} R_{11}^{(t)}\,\mathrm{d}r$$

and

$$\varLambda_{11}^{(t)} = \int_0^{\tau(R_{11}^{(t)}=0)} R_{11}^{(t)}\,\mathrm{d}\tau$$

are presented instead.

Figure 18 displays profiles of the integral timescale $\varLambda_{11}^{(t)}$ of the longitudinal velocity fluctuations along the centreline of the splitter plate. While there is some variation in the normal direction in the upstream part of the reversed-flow region, the profiles of $\varLambda_{11}^{(t)}$ become almost flat, beginning at about $x/x_R = 0.6$. Figure 19 shows the development of the integral timescale along the line of the maximum longitudinal fluctuation intensity. $\varLambda_{11}^{(t)}$ rises rapidly in the first quarter of the reverse-flow region and reaches a plateau near reattachment, implying that the energy-carrying structures do not grow further but are simply convected through the reattached flow field. These integral timescales were measured as suggested by Castro (1985) and agree very well with those presented by Castro & Haque (1987).

Since the integral lengthscales were measured using hot wires only, no data are available in the reverse-flow region. Profiles of the integral lengthscales $\varLambda_{11}^{(2)}$ and $\varLambda_{11}^{(3)}$ were measured at several stations along the centreline. Owing to space limitations the full profiles are not presented here but they confirm in more detail the trends found by RF. To illustrate the general behaviour, figures 20 and 21 show the development of the two integral lengthscales at two characteristic loci of the flow: at the outer edge of the separated mixing layer (y where $T_u = 10\%$), and at the centre of the layer (y where $\overline{u'^2}$ has a maximum). The values of $\varLambda_{11}^{(2)}$ and $\varLambda_{11}^{(3)}$ rise almost monotonically along the locus of $y_{\overline{u^2_{max}}}$, with $\varLambda_{11}^{(2)}$ always larger than $\varLambda_{11}^{(3)}$, showing
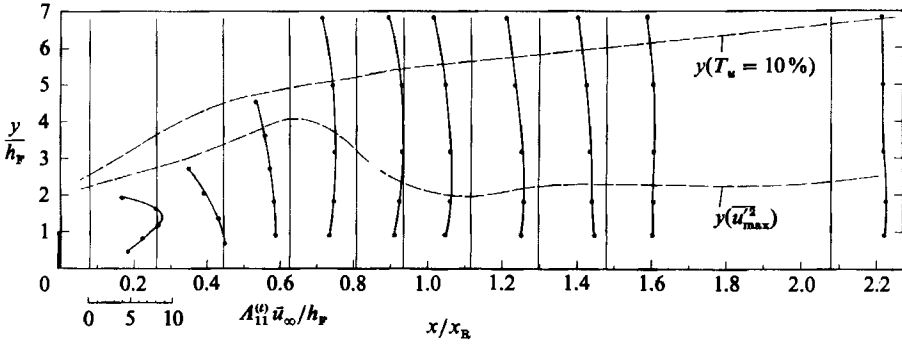
FIGURE 18. Profiles of the integral timescale $A_{11}^{(t)}$ along the centreline of the splitter plate (pulsed-wire data).
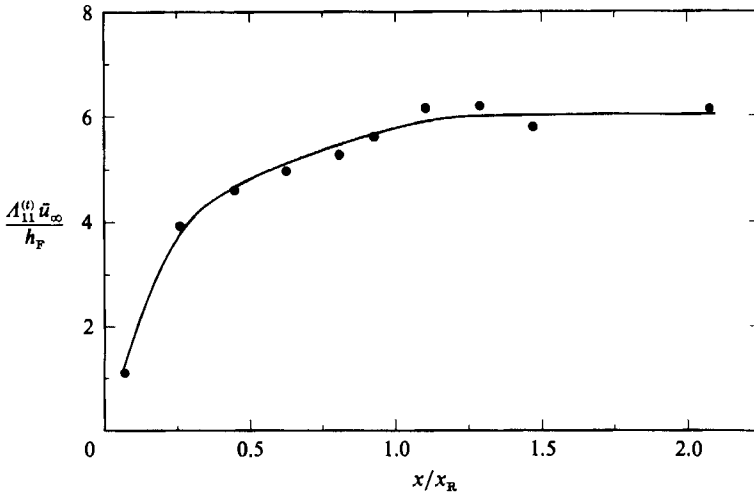

FIGURE 19. Development of the integral timescale $A_{11}^{(t)}$ along the locus of $\overline{u_{max}'^2}$ against x/x_R.
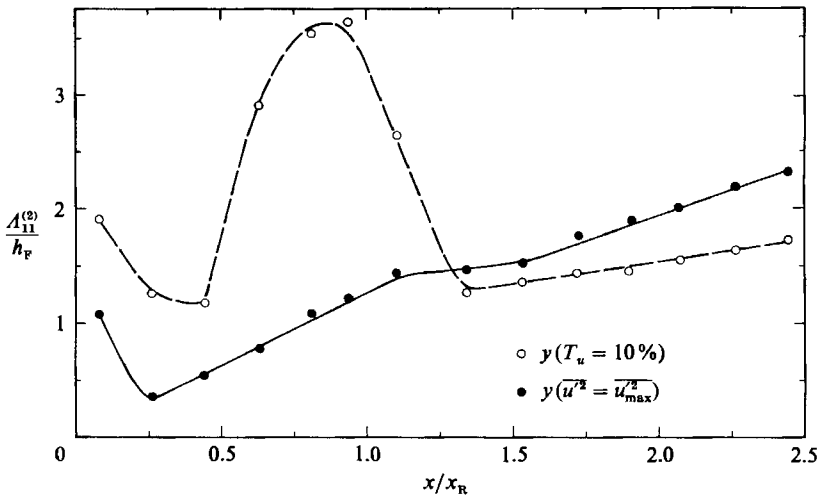

FIGURE 20. Development of the integral lengthscale $A_{11}^{(2)}$ along the locus of $\overline{u_{max}'^2}$ and the locus of $T_u = 10\%$ against x/x_R.
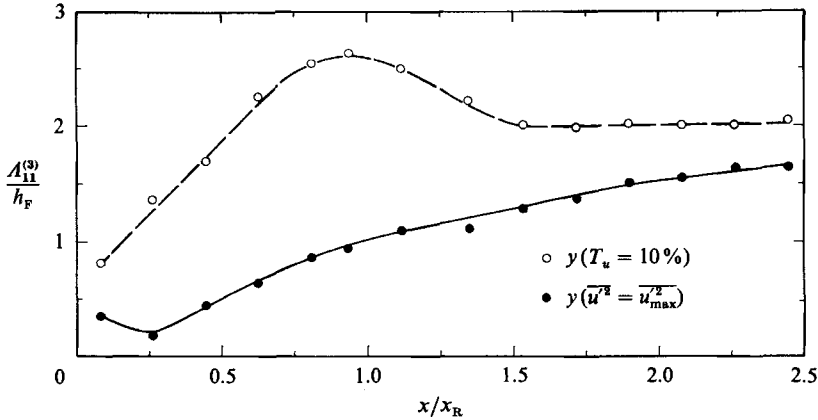
FIGURE 21. Development of the integral lengthscale $\Lambda_{11}^{(3)}$ along the locus of $\overline{u'^2_{\max}}$ and the locus of $T_u = 10\%$ against x/x_R.

the limited spanwise extent of the large-scale structures. Along the locus of $T_u = 10\%$ both lengthscales peak dramatically near reattachment. $\Lambda_{11}^{(2)}$ subsequently falls off sharply owing to the wall constraint in the reattached shear layer, whereas $\Lambda_{11}^{(3)}$ decreases more gradually. For the spanwise behaviour of the profiles of the integral lengthscales the reader is referred to Jaroch (1987 a).

3.5. *Power spectral densities and coherence*

Using hot-wire anemometry we have investigated the spectral properties of u'. The power spectral density function

$$S_{11}(\omega) = \int_{-\infty}^{\infty} R_{11}^{(t)} \, e^{i\omega t} \, d\tau$$

provides the fluctuating kinetic energy at a specific frequency. The coherence is defined as

$$\gamma_{11_{ab}}(\omega) = \left(\frac{|S_{11_{ab}}(\omega)|^2}{S_{u_a}(\omega) \, S_{u_b}(\omega)} \right)^{\frac{1}{2}}.$$

Here $S_{11_{ab}}(\omega)$ denotes the cross-spectral density of two signals u'_a and u'_b measured at two different positions a and b in the flow. The coherence is a measure of the correlation at a specific frequency ω.

Measurements of $S_{11}(\omega)$ in the empty test section showed no specific peaks that could be characteristic of harmonic changes of the volume flow due to separation in the wind tunnel. Figure 22 presents the development of S_{11} at a fixed height above the centreline of the splitter plate at different positions x/x_R. The two upstream distributions, with the separated shear layer lying below the measuring stations, are characterized by low-frequency fluctuations, whereas further downstream fluctuations at higher frequency become more important. Beyond the mean reattachment point little change occurs in the power spectral density distribution.

Since Castro & Haque (1987) measured a dominating frequency of about 24 Hz $(0.12u_\infty/x_R)$ in their flow configuration and interpreted it as the 'flapping frequency' of the separated shear layer, we checked the flow of the present experiment for the occurrence of a similar effect. Figure 23 presents one example of the power spectral density function in the frequency range $0.25 < f < 50$ Hz. Here, as with all other
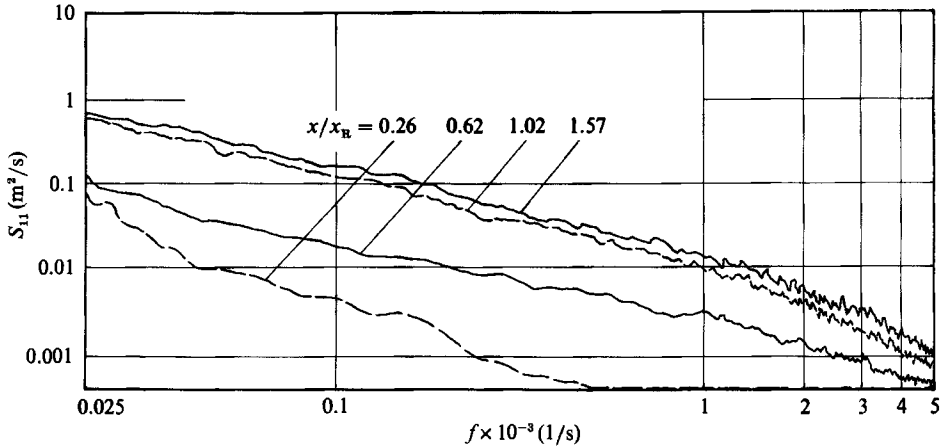
FIGURE 22. Development of the power spectral density S_{11} at $y/h_F = 4.55$ along the centreline of the splitter plate.
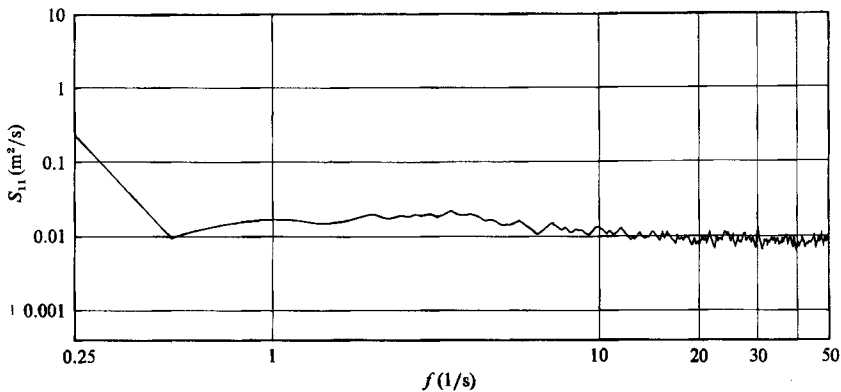

FIGURE 23. Power spectral density S_{11} at $x/x_R = 0.26$ and $y/h_F = 3.18$ on the centreline in the reverse-flow region.

spectra measured, no low-frequency peak could be observed. This result is in accordance with RF and based on several hundred measured spectra.

The development of the coherence at $x/x_R = 0.2$ and $y/h_F = 3.18$ with different spanwise separations of the two probes is shown in figure 24. The fixed probe was positioned above the centreline of the splitter plate, and it is observed that the high-frequency content of the signals contributing to the coherence decreases rapidly with increasing spanwise separation. Even at small spatial separation it is only the larger structures with frequencies below 200 Hz that contribute to the coherence.

3.6. Measurements in the spanwise direction

Since we could not perform a complete parameter study to separate the effects of aspect ratio and sidewall boundary layer/horseshoe vortex interaction on the flow field, it is not possible to discuss these effects separately. We do think, however, that the present experiment is typical of the type of flow over a T-shaped configuration and demonstrates which turbulence quantities are affected most by the three-dimensionality of the flow.

Owing to space limitations only a small fraction of the spanwise data can be
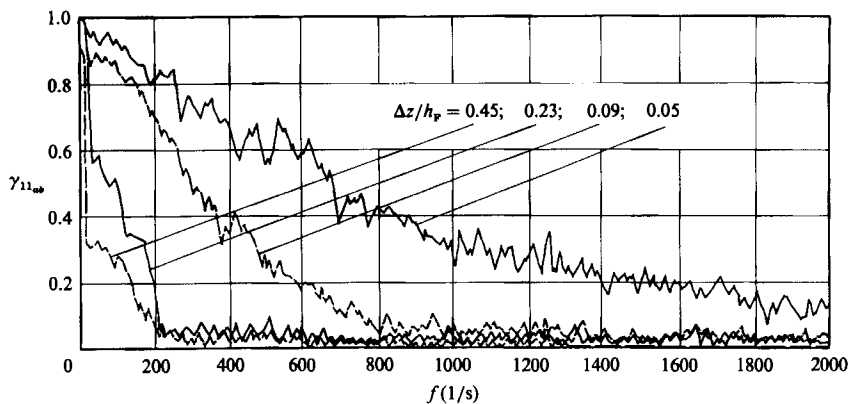
FIGURE 24. Development of the coherence at $x/x_R = 0.2$ and $y/h_F = 3.18$ on the centreline of the splitter plate.
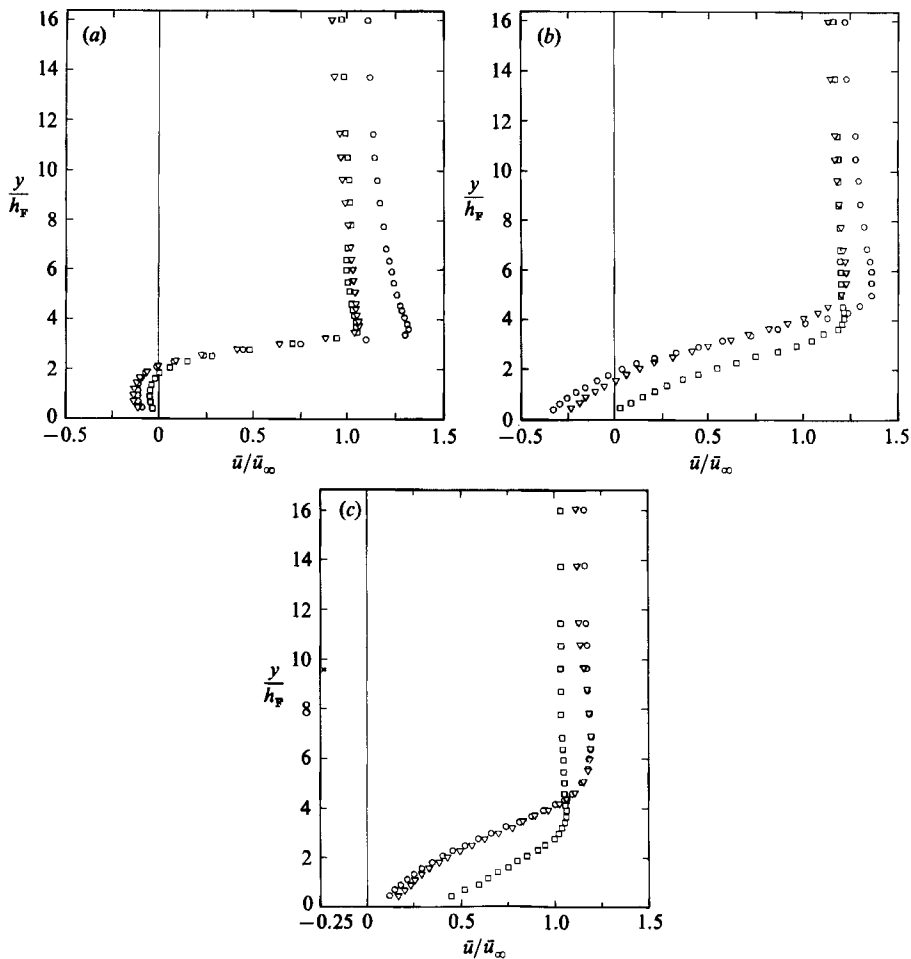

FIGURE 25. Distributions of the mean velocity $\bar{u}$ at (a) $x/x_R = 0.2$, (b) 0.56 and (c) 0.92 and three spanwise positions: $\bigcirc$, $z/(\frac{1}{2}B) = -0.286$; $\bigtriangledown$, -0.571; $\square$, -0.857.
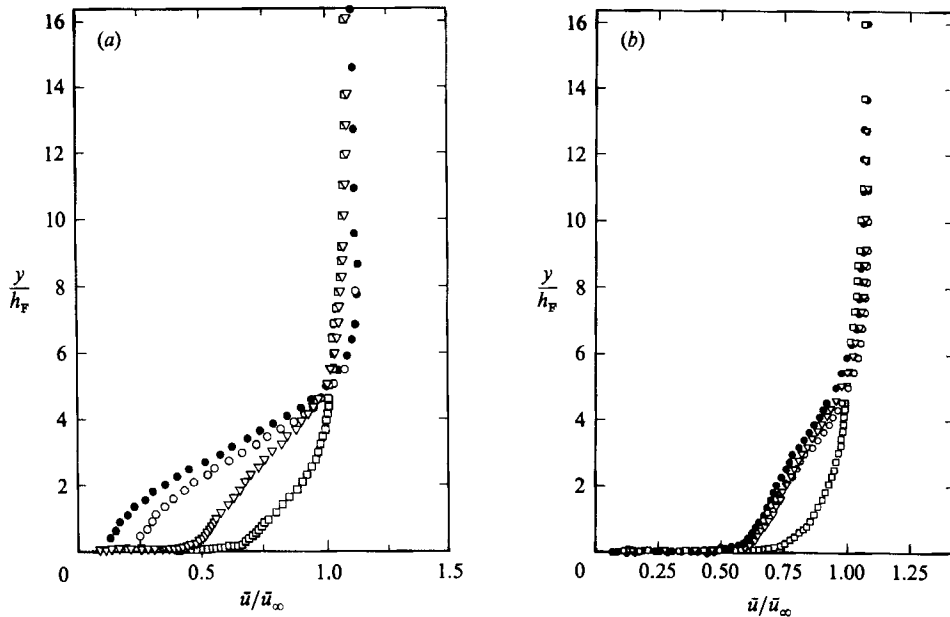
FIGURE 26. Distributions of the mean velocity $\bar{u}$ at (a) $x/x_{\mathrm{R}} = 1.09$ and (b) 1.45 and four spanwise positions: ●, $z/(\frac{1}{2}B) = 0$; ○, -0.286; ▽, -0.571; □, -0.857.

presented. For a more detailed description the reader is again referred to Jaroch (1987a). They show that even a flow with relatively large aspect ratio and low blockage is severely influenced by secondary flow. The distributions of the mean-velocity components and the Reynolds shear and normal stresses show three-dimensional effects both in the distributions of the magnitude of their maxima and in the shape of the profiles in the spanwise direction. Even if profiles of a given quantity are compared not at identical positions downstream of separation but rather at identical positions in terms of the local bubble length, the profiles do not collapse onto each other.

Figures 25 and 26 show the spanwise variation of the mean velocity profiles for five positions downstream of separation. Except at $x/x_{\mathrm{R}} = 0.2$, profiles near the sidewall (squares) are clearly distinct from those at other spanwise positions for $y/h_{\mathrm{F}} < 4$. They are strongly influenced both by the system of horseshoe vortices at the splitter plate/sidewall junction and by the wind-tunnel wall boundary layer. No profile shows an inflection after $x/x_{\mathrm{R}} = 0.56$.

There were no measurement ports on the centreline at the three positions of the splitter plate in the reverse-flow region, so the figures do not contain data at $z/(\frac{1}{2}B) = 0$ at these stations; however, the profiles at $z/(\frac{1}{2}B) = 0.286$ are representative of those on the centreline. The changes between the profiles denoted by the circles and triangles between $x/x_{\mathrm{R}} = 0.92$ and 1.09 indicate a faster reattachment of the flow further away from the centreline. Figure 25 also clearly displays the flow retardation near the tunnel sidewall (squares) in the separated shear layer $(y/h_{\mathrm{F}} > 4)$. Readjustment to nominally two-dimensional behaviour appears to be achieved at about $0.5x_{\mathrm{R}}$ downstream of reattachment. However, this is not the case for the turbulence quantities, and even the mean velocity profiles themselves, when scaled with inner (wall) variables (figure 27), continue to show three-dimensionality as far downstream as $2.38x_{\mathrm{R}}$ (see figure 14).
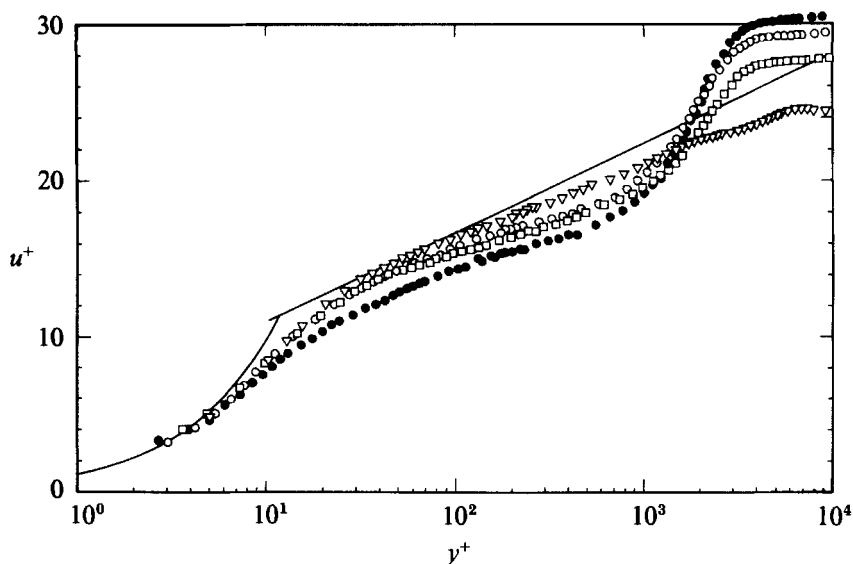
FIGURE 27. Distributions of the mean velocity $\bar{u}$ in inner coordinates at $x/x_R = 1.45$ and four spanwise positions. Symbols as figure 26.
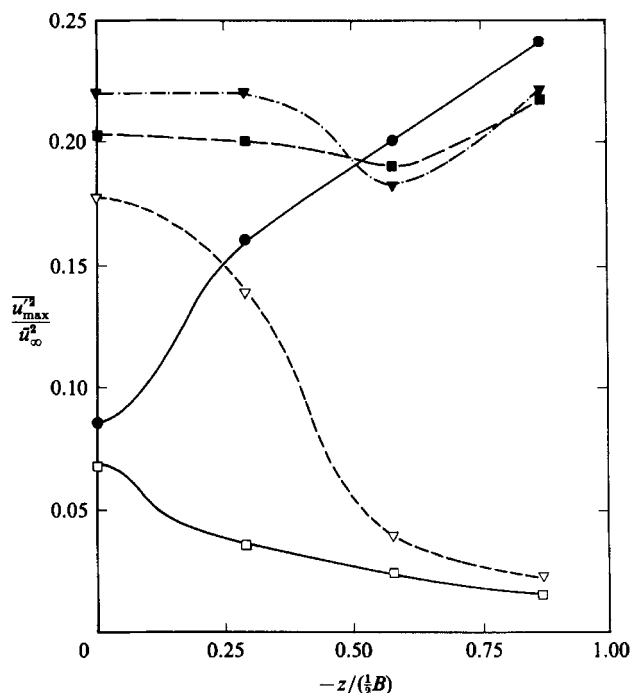

FIGURE 28. Spanwise distributions of the maximum of the longitudinal fluctuation intensity $\overline{u'^2}$: ●, $x/x_R = 0.20$; ▼, 0.56; ■, 0.92; ▽, 1.09; □, 1.45.

The three-dimensional behaviour of the Reynolds stresses is indicated by the spanwise variation in the maximum values of $\overline{u'^2}$ and $\overline{u'v'}$ at five downstream positions, presented in figures 28 and 29, respectively. The strongest variation in the maxima of $\overline{u'^2}$ and $\overline{u'v'}$ occurs immediately downstream of reseparation ($x/x_R = 0.2$) and at reattachment. Except near reseparation, the longitudinal fluctuation intensity
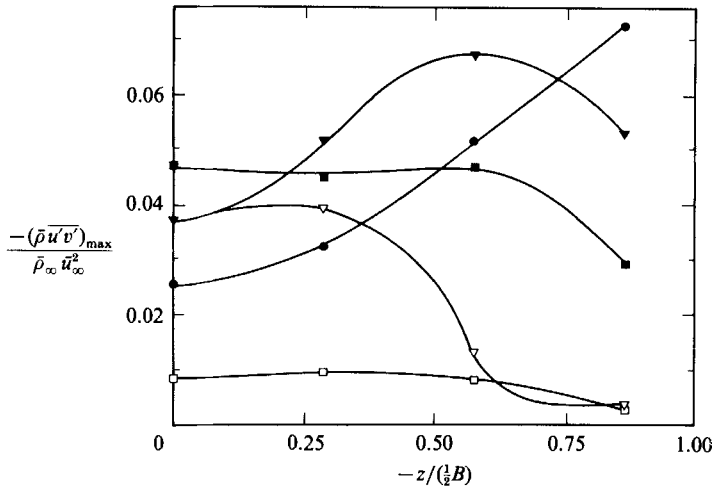
FIGURE 29. Spanwise distributions of the maximum of the Reynolds shear stress $\overline{\rho u'v'}$. Symbols as figure 28.

(figure 28) is highest along the centreline, and within the reverse-flow region fluctuations of about the same level are generated near the sidewall by the interaction of the corner flow and the shear layer. The same pattern holds for the component $(\overline{u'v'})_{\mathrm{max}}$ of the Reynolds shear stress. Just downstream of reattachment $x/x_{\mathrm{R}\mathbb{C}} = 1.09$ (open triangles), the Reynolds stresses near the sidewall fall to approximately one-quarter of the centreline levels. This indicates the strong damping effect on the turbulence which accompanies the early reattachment induced by the sidewall (cf. figure 6). A comparison of figures 4, 7, 28 and 29 shows that spanwise uniformity is achieved first by the static pressure, then by $\overline{u'v'}$, and furthest downstream by the skin friction and the Reynolds normal stress component $\overline{u'^2}$. Since measurements of the components of the Reynolds stress tensor are still rare in reverse-flow regions, figure 30 shows profiles of the normal stresses at several spanwise locations and figure 31 shows $\overline{u'v'}$ and $\overline{u'w'}$. These figures prove a clearly three-dimensional behaviour, with distinctly different profiles on the centreline and near the sidewall. The profile peaks of $\overline{u'^2}$ and $\overline{v'^2}$ increase near the sidewalls owing to the strong mixing in this region, whereas the sidewall exerts a strong damping on $\overline{w'^2}$.

The profiles of $\overline{u'v'}$ confirm the trend indicated by the distribution of the maxima in figure 29 (filled triangles) with the maximum value at $z/(\frac{1}{2}B) = -0.571$.

The component $\overline{u'w'}$ (figure 31) is the smallest Reynolds shear stress, with a peak value of about 8% of that of $\overline{u'^2}$, and shows a strong variation in the spanwise direction including a change of sign. Further downstream ($x/x_{\mathrm{R}} = 1.09$) the negative sign, characteristic of the distribution in the outer part of the flow, extends down to the wall. Downstream of reattachment $\overline{u'w'}$ decreases rapidly towards zero, as it should for two-dimensional flow (for a more detailed discussion see Jaroch 1987a).

4. Conclusions

Detailed pulsed-wire measurements of skin friction, velocity, and Reynolds stresses in the reverse-flow region of a normal plate with a long splitter plate have revealed the three-dimensional character of this type of flow. Large spanwise
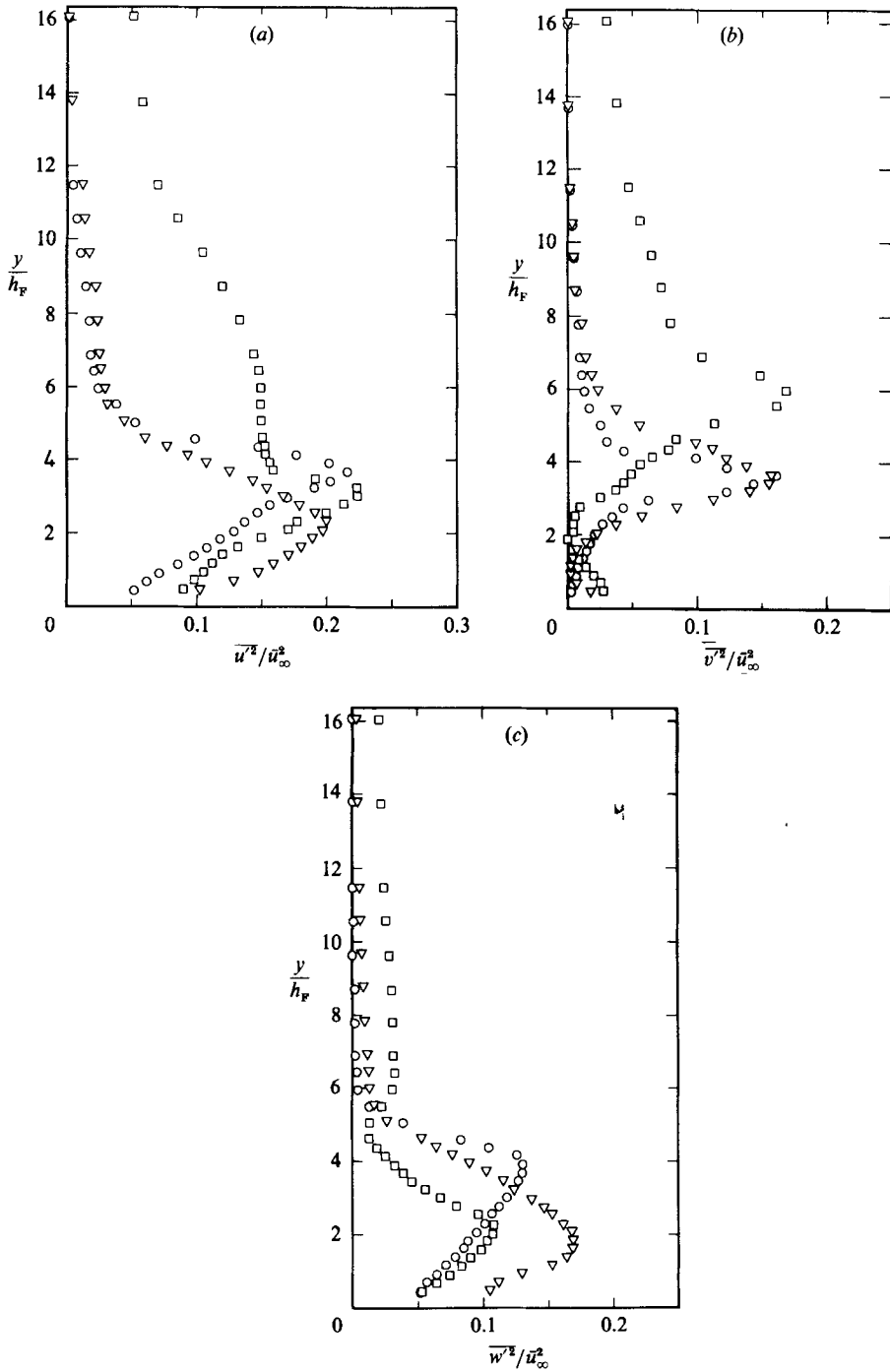
FIGURE 30. Profiles of the intensity of the fluctuating velocities (a) u', (b) v' and (c) w' at $x/x_R = 0.56$ and three spanwise positions: $\bigcirc$, $z/(\frac{1}{2}B) = -0.286$; ∇, -0.571; $\square$, -0.857.
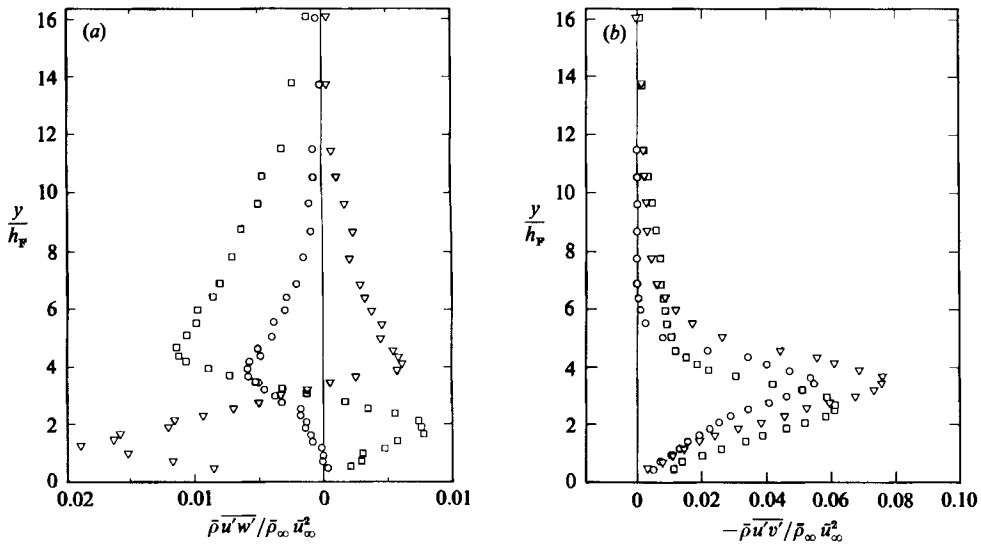
FIGURE 31. Profiles of the components (a) $\overline{u'v'}$ and (b) $\overline{u'w'}$ of the Reynolds shear stress at $x/x_{\mathrm{R}} = 0.56$ and three spanwise positions. Symbols as figure 30.

variations of mean velocity and of five components of the Reynolds stress tensor have shown that the shape of the reverse-flow region is longer and higher along the centreline of the splitter plate, and it shortens and flattens towards the tunnel sidewalls. This three-dimensional behaviour of the flow occurs even though tunnel blockage and the turbulence level of the free stream are lowest and the aspect ratio highest among the published cases of this type of configuration. End plates were found to weaken the three-dimensionality in some cases but could not eliminate it. Increasing the aspect ratio A by a factor of 3 and decreasing blockage by a factor of 2 approximately doubles the maximum values of $\overline{u'^2}$ and $\overline{u'v'}$ and triples those of $\overline{v'^2}$ and $\overline{w'^2}$ along the centreline in the reverse-flow region. The influence of these two parameters appears to dominate that of the sidewall boundary layer. However, the sidewall boundary layers do appear to change the nature of the three-dimensionality close to the sidewalls, as demonstrated by the differences in the profiles of the mean and fluctuating quantities. In the upstream part of the reverse flow near the sidewall region the turbulence intensities were, for example, distinctly larger than those near the centreline, which may be explained by the interaction between the shear layer and the system of horseshoe vortices. These vortices apparently induce highly correlated fluctuations, resulting in high Reynolds shear stresses.

Measurements of the correlation coefficients of the longitudinal turbulent fluctuation u' show that the turbulent structures have correlation lengthscales in the spanwise direction that are not significantly higher than those measured in the other directions. This permits the conclusion that the turbulent energy-carrying structures have finite spanwise extent.

Low-frequency flapping of the separated shear layer does not occur in the present experiment, since peaks were not observed in extensive measurements of power spectral densities. Thus, the observed increase in turbulence activity, indicated both by the turbulence intensities and by the shear stresses, cannot be accounted for by a fixed frequency flapping of the shear layer; however, such flapping may occur as a rare stochastic phenomenon. A comparison with experimental results obtained in

other turbulent shear flows of a similar geometry leads to the conclusion that flow parameters such as aspect ratio, wind-tunnel blockage, and presumably free-stream turbulence intensity influence the reattachment length, the bubble slenderness, and the level of the turbulence fluctuation intensities. Reverse-flow regions obtained in 'low-interference' experiments are long and high, with high fluctuation intensities.

These experimental results confirm the conclusion from numerical experiments using the discrete-vortex method (Jaroch & Graham 1988) that the flow around the configuration investigated by RF cannot be assumed to be nominally two-dimensional. Models that do not take into account three-dimensional effects should therefore give physically incorrect answers.

REFERENCES

ADAMS, E. W., JOHNSTON, J. P. & EATON, J. K. 1984 Experiments on the structure of a turbulent reattaching flow. *Rep.* MD-43. Stanford University, Stanford, CA.

BRADBURY, L. J. S. & CASTRO, I. P. 1971 A pulsed wire technique for velocity measurements in highly turbulent flows. *J. Fluid Mech.* **49**, 657–691.

BREDERODE, V. A. S. L. DE 1975 Three-dimensional effects in nominally two-dimensional flows. Ph.D. thesis, Imperial College of Science and Technology, University of London.

CASTRO, I. P. 1985 Time-domain measurements in separated flows. *J. Fluid Mech.* **150**, 183–201.

CASTRO, I. P. & CHEUN, B. S. 1982 The measurement of Reynolds stresses with a pulsed wire anemometer. *J. Fluid Mech.* **118**, 45–58.

CASTRO, I. P. & DIANAT, M. 1983 Surface flow patterns on rectangular bodies in thick boundary layers. *J. Wind. Engng Ind. Aerodyn.* **11**, 107–119.

CASTRO, I. P. & HAQUE, A. 1987 The structure of a turbulent shear layer bounding a separated region. *J. Fluid Mech.* **179**, 439–468.

CHERRY, N. 1982 The effects of stream turbulence on a separated flow with reattachment. Ph.D. thesis, Dept. of Aeronautics, Imperial College of Science and Technology, University of London.

CHERRY, N. J., HILLIER, R. & LATOUR, M. E. M. P. 1984 Unsteady measurements in a separated and reattaching flow. *J. Fluid Mech.* **144**, 13–46.

DENGEL, P., FERNHOLZ, H. H. & HESS, M. 1987 Skin-friction measurements in two- and three-dimensional highly turbulent flows with separation. *Proc. 1st European Turbulence Conf.* (ed. J. Mathieu & G. Comte Bellot). Springer.

EATON, J. K. & JOHNSTON, J. P. 1981 A review of research on subsonic turbulent flow reattachment. *AIAA J.* **19**, 1093–1100.

FERNHOLZ, H. H. & VAGT, J. D. 1981 Turbulence measurements in an adverse-pressure-gradient three-dimensional turbulent boundary layer along a circular cylinder. *J. Fluid Mech.* **111**, 233–270.

FROEBEL, E. & VAGT, J.-D. 1974 Ein automatisch abgleichendes Flüssigkeitsmanometer mit digitaler Anzeige. *DFVLR FB* 74–80.

HANCOCK, P. E. 1980 The effect of free-stream turbulence on turbulent boundary layers. Ph.D. thesis, Imperial College of Science and Technology, University of London.

HILLIER, R., LATOUR, M. E. M. P. & CHERRY, N. J. 1983 Unsteady measurements in separated and reattaching flows. *4th Turbulent Shear Flow Conf., Karlsruhe.* Springer.

JAROCH, M. 1985 Development and testing of pulsed wire probes for measuring fluctuating quantities in highly turbulent flows. *Exp. Fluids* **3**, 315–322.

JAROCH, M. 1987*a* Eine kritische Betrachtung der Methode diskreter Wirbel als Modell für eine abgelöste Strömung mit geschlossener Ablöseblase auf der Basis experimenteller Erkenntnisse. Dissertation, Hermann-Föttinger-Institut für Thermo- und Fluiddynamik, Technische Universität Berlin.

JAROCH, M. 1987*b* Oil flow visualization experiments in the separated and reattaching flow past a normal flat plate with a long wake splitter plate. *Z. Flugwiss.* **11**, 230–236.

JAROCH, M. & DAHM, A. 1987 A new pulsed-wire probe for measuring the Reynolds stresses in the plane containing the main shear direction of a turbulent flow. *Internal Rep.* IB 01/87. Hermann-Föttinger-Institut für Thermo- und Fluiddynamik, Technische Universität Berlin, Berlin.

JAROCH, M. & GRAHAM, J. M. R. 1988 An evaluation of the discrete vortex method as a model for the flow past a flat plate normal to the flow with a long wake splitter plate. *J. Méc. Theor. Appl.* **7**, 105–134.

KIYA, M. & SASAKI, K. 1983 Structure of a turbulent separation bubble. *J. Fluid Mech.* **137**, 83–113.

KIYA, M. & SASAKI, K. 1985 Structure of large-scale vortices and unsteady reverse flow in the reattaching zone of a turbulent separation bubble. *J. Fluid Mech.* **154**, 463–491.

KIYA, M., SASAKI, K. & ARIE, M. 1982 Discrete-vortex simulation of a turbulent separation bubble. *J. Fluid Mech.* **120**, 219–244.

LATOUR, M. E. M. P. 1983 The effect of geometry and stream turbulence on separated flows. Ph.D. thesis, Imperial College of Science and Technology, University of London.

NAKAMURA, Y. & OZONO, S. 1987 The effects of turbulence on a separated and reattaching flow. *J. Fluid Mech.* **178**, 477–490.

OTA, T. & ITASAKA, M. 1976 A separated and reattached flow on a blunt flat plate. *Trans. ASME* I: *J. Fluids Engng* **98**, 79–86.

ROSHKO, A. & LAU, J. C. 1965 Some observations on transition and reattachment of a free shear layer in incompressible flow. *Proc. 1965 Heat Transfer and Fluid Mech. Inst.*

RUDERICH, R. 1985 Entwicklung des Nachlaufs einer senkrechten Platte längs einer zur Anströmung parallelen ebenen Wand. Dissertation, Hermann-Föttinger-Institut für Thermo- und Fluiddynamik Technische Universität Berlin, Berlin.

RUDERICH, R. & FERNHOLZ, H. H. 1986 An experimental investigation of a turbulent shear flow with separation, reverse flow, and reattachment. *J. Fluid Mech.* **163**, 283–322 (referred to as RF).

SMITS, A. J. 1982 Scaling parameters for a time averaged separation bubble. *Trans. ASME* I: *J. Fluids Engng* **104**, 178–184.

WAGNER, P.-M. 1986 Entwicklung eines verbesserten Pulsdrahtanemometers zur Erfassung von Geschwindigkeiten und Korrelationen in turbulenten Strömungen. Diplomarbeit, Herman-Föttinger-Institut für Thermo- und Fluiddynamik TU Berlin, Berlin.